Performance predictions of the SPARC X-ray crystal spectrometers for ion temperature and toroidal rotation measurements

C. Perks,[1] D. Vezinet,[2] J.E. Rice,[1] and M.L. Reinke[2]
[1)] *Plasma Science and Fusion Center, Massachusetts Institute of Technology, Cambridge, Massachusetts 02139, USA*
[2)] *Commonwealth Fusion Systems, Devens, Massachusetts 01434, USA*

(*Electronic mail: cjperks@psfc.mit.edu)

(Dated: 6 August 2024)

SPARC will be outfitted with three systems of X-ray crystal spectrometer arrays. Two of these are designed using cylindrically bent crystals to achieve high spectral-resolution for ion temperature and toroidal velocity measurements via imaging He-like Kr and Ne-like Xe. The last acts as a spectral survey system to monitor Ne-like W and nearby H- and He-like emission from Cr, Fe, Co, Ni, Cu. Line radiation intensities are calculated using the FLEXIBLE ATOMIC CODE for atomic data and COLRADPY for collisional-radiative modeling then convoluted with a Voigt line shape. Free-free, free-bound, and two-photon continuum radiation is also included. The TOFU code is used to perform volume-of-sight integration to produce synthetic detector images. Also presented is cross-validation performed using the XICSRT Monte Carlo ray-tracing code. Ion temperature and toroidal velocity profiles are reconstructed using TOFU via tomographic inversion.

I. INTRODUCTION

Fusion power plants (FPP's) are expected to operate in novel regimes of electron/ion temperature. To optimize the DT fusion reactivity, plasmas need to reach 10–20 keV. Estimates of the toroidal rotation velocity are order of 100 km/s[1–3]. It is therefore important to have reliable measurements of these quantities to benchmark predictions and provide feedback in the control room.

X-ray crystal spectroscopy (XRCS) will be employed on the SPARC tokamak[4], currently under construction, to provide such measurements. XRCS is a class of Bragg spectrometers that utilizes a crystal for the dispersive element as the small lattice spacing is of the order suitable to diffract X-ray wavelengths. The inherent almost Delta function-like reflectivity (rocking curve) of a crystal allows for high resolving power passive spectroscopy[5]. The exact wavelength of interest constrains the Miller plane the crystal needs to be cut at.

A carefully selected trace impurity is imaged to observe the Doppler broadening and shift of characteristic electronic transitions from high ionization states. This impurity is usually either a seeded noble gas[6–8], such as Ar, Kr, Xe, or intrinsically present[9–12], such as Fe, Mo, W. Typically, closed-shell charge states are utilized to maximize signal over a wide electron temperature range. Another benefit of closed-shell charge states is that the atomic structure is easier to calculate.

This paper summarizes performance predictions of this diagnostic to validate the design. Section II introduces the design of three sets of spectrometers, each with their own specialization. Section III describes and justifies the synthetic diagnostic modeling performed. Section IV details the atomic data modeling. Section V then introduces a method we are exploring to reconstruct ion temperature and toroidal rotation radial profiles. Section VI then concludes with future work.

II. DIAGNOSTIC DESIGN

Because of the large dynamic range of the electron temperatures FPP's are projected to operate in (1–20 keV), no single impurity charge state has sufficient abundance to provide full coverage as has been the role of He-like Ar in modern tokamaks[13,14]. As such, it was deemed necessary to have two sets of spectrometers, one dedicated to low temperature regions of the plasma and another for high temperature. Numerous candidate lines have been considered in literature from similar FPP XRCS design papers[15–19]. We have elected to rely on Ne-like Xe to diagnose an electron temperature range of 4–9 keV and He-like Kr for 10–20 keV. Figure 1 illustrates this decision from an argument of emissivity per radiated power (hence agnostic to electron density or impurity concentration) from the brightest line of each charge state. It should be noted here that there are known issues with the atomic data utilized which will be described in more detail in Section IV.

It was determined desirable to implement a third system to act as a low-resolution survey of highly ionized (He-, H-like) common industrial metals (Cr, Fe, Co, Ni, Cu) as well as close Ne-like W lines. Throughout this paper, we will denote these three systems as XRS-HR-Kr, XRS-HR-Xe, XRS-LR where XRS means X-Ray Spectrometer, HR means High-Resolution, and LR means Low-Resolution.

An important design constraint for all SPARC diagnostics is the expected intense neutron fluxes. Other FPP XRCS designs have chosen to approach this problem by implementing grazing incidence mirrors[19]. For SPARC, we have decided not to do the same in favor of simplifying alignment with less optical elements. We therefore could not use a spherical Johann configuration as the aperture required would be too big. Most SPARC diagnostics are located about 16 m away from the tokamak behind a thick concrete wall. The beamline diameter is 10 cm meaning that for a spectrometer with a slit, the volume-of-sight through the plasma is very narrow. Thus, an array of spectrometers is needed to cover the poloidal plane.

TABLE I. Characteristics of the crystals selected for each spectrometer system. λ_0 is the central reflected wavelength for each crystal choice with θ_B and R_{int} being the resultant Bragg angle and integrated reflectivity, respectively[22,23].

	XRS-HR-Kr	XRS-HR-Xe	XRS-LR
Crystal	Ge(242)	Qz(101)	Ge(202)
λ_0 [Å]	0.945	2.72	1.62 (1.42-1.81)
θ_B [degree]	24.2°	24.0°	24.0°
R_{int} [μrad]	12.7	32.7	63.3

A spectrometer for each system (XRS-HR-Kr, XRS-HR-Xe, XRS-LR) is housed within a common beamline. Figure 2 illustrates how per beamline, there is a vertical stack of three crystals for each respective system that reflect an image onto a large common camera. Due to the port space available, up to 5 beamlines can be installed. See the accompanying paper in these proceedings[20] for more information.

Table I details the crystal chosen for each spectrometer system. Care was taken to select the highest integrated reflectivity, and hence throughput, while not costing spectral resolution by an angular width significantly larger than candidate detector pixels. This typically implies choosing Ge crystals over Quartz for the same Bragg angle. The crystals will be bent cylindrically typical of von Hámos configurations[6,21].

The notable difference of our design to the von Hámos configuration is that space constraints in the diagnostic lab forced us to compactify by forgoing the vertical focus. Moving the slit light source off the principal axis of the reflector causes the image rays to be divergent. This though allows one to move the detector closer from the center of curvature towards the focal point. This also means that the crystal radius of curvature is now a free variable. For a particular crystal-to-detector distance, decreasing the radius of curvature starting from a flat crystal conically bends and compactifies a flat image at the cost of spectral resolution at the image top/bottom from a wider wavelength integration per pixel. An example of such image for radius, $R = 0.6$ m is given in Section V. The exact radius of curvature for each crystal is being chosen to ensure each spectra can be measured on a common detector per beamline.

The distance from the port face on SPARC to the limiting slit is 11.5 m, the distance from the slit to the crystal is 4.4 m, and the distance from the crystal to the detector is 0.4 m. Note that two slits will be installed along the field-of-view to act as a double barrier for tritium. Be is the traditional window material for its good X-ray transmission, but we are scoping using diamond instead. Diamond has a lower X-ray transmission, but better toxicity, neutron, and tritium properties, as well as simpler procurement, while possibly making a thinner window. Diamond being transparent to visible light also allows for easier alignment. The particular dimensions of the optics, such as slit size, is in progress of being optimized for photon flux and ease of analysis.

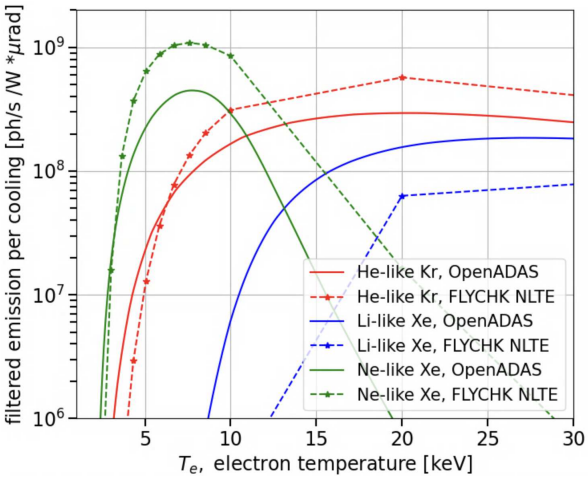

FIG. 1. Calculated emissivity rate per the impurity's cooling rate as a function of T_e at $n_e = 1e14$ cm^{-3} for proposed diagnostic X-rays on FPPs. Charge state distributions were calculated either using OpenADAS or FLYCHK's NLTE model[24], so assuming coronal ionization balance (no transport). Emissivity was calculated using FAC/ColRadPy as described in Section IV. Energy-dependent filtering was also included using a 50μm diamond window, associated crystal reflectivity (used Qu(101), $R_{int} = 30\mu$rad for Li-like Xe), and detector quantum efficiency of 60% for Xe and 90% for Kr.

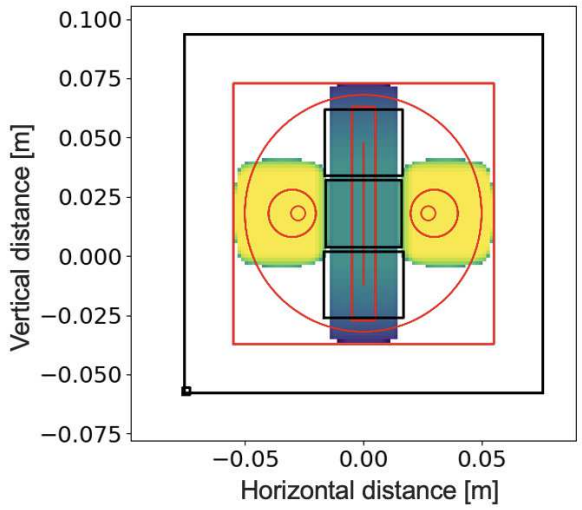

FIG. 2. Projection of the optics along a beamline looking towards the crystals. The largest red circle outlines the beamline diameter and in black are outlined the crystals. Outlined in red within the beamline are the apertures depicting that there will be either a single common or three individual slits with pinholes for other diagnostics on each side. Note the double barrier along the field-of-view. The heat map illustrates the geometric étendue through the apertures.

III. SYNTHETIC DIAGNOSTIC MODELING

The main tool we use to simulate and analyze synthetic diagnostics is the ToFu code[25]. In this work, we utilize provided tools for volume-of-sight integration, tomographic inversions, rocking curve calculations, and deterministic ray-

tracing. These particular tools were developed to analyze XRCS spectra measured on the WEST tokamak which is a spherical Johann-type imaging spectrometer[14]. As suggested in Section II, an addition to the code had to be made for cylindrically curved crystals for this work.

It is important to us that our performance projections for this diagnostic are reliable, so we are in the progress of cross-validating our photon flux calculations with another popular ray-tracing code, XICSRT, which is a Monte Carlo-type calculation. XICSRT has been benchmarked against other codes for a spherical Johann-type spectrometer to great success[19,26]. Still novel though are cylindrical reflections which are in progress of being implemented.

For both codes, rocking curves for each combination of wavelength and crystal simulated are calculated using TOFU. Used are equations from dynamical diffraction theory, here assuming a finite sized, perfect crystal at 25°C[22,23]. Models in TOFU are included to account for thermal expansion and mosaicity, but are not utilized here.

Our validation exercise consists of comparing photon flux distributions calculated for a 1) mono-energetic point source, 2) mono-energetic volumetric source, 3) multi-energy volumetric source, and 4) including a flux function velocity profile. Each of these cases will be simulated for 1) an example spherical Johann spectrometer, 2) an example von Hámos spectrometer, and 3) the as-designed spectrometer layout described in Section II.

At the time of writing this paper, only the case of a mono-energetic point source imaged by a spherical crystal spectrometer has been completed. The example spectrometer views the SPARC midplane with a port-to-aperture distance of 11.5 m, a aperture-to-crystal distance of 4.4 m, and a crystal-to-detector distance of 0.4 m. The aperture has width/height of 5 mm/4 cm, the crystal has a width/height of 3.0 cm/8.5 cm and a radius of curvature of 0.4 m, and the detector has a width/height of 1.3 cm/0.7 cm. The source is isotropic with a wavelength of 1.61 Å and an emissivity of 1 ph/s/srad. Figure 3 illustrates that both codes calculate the same detector image both in terms of the number of photons detected and the distribution within ray-tracing Poisson error.

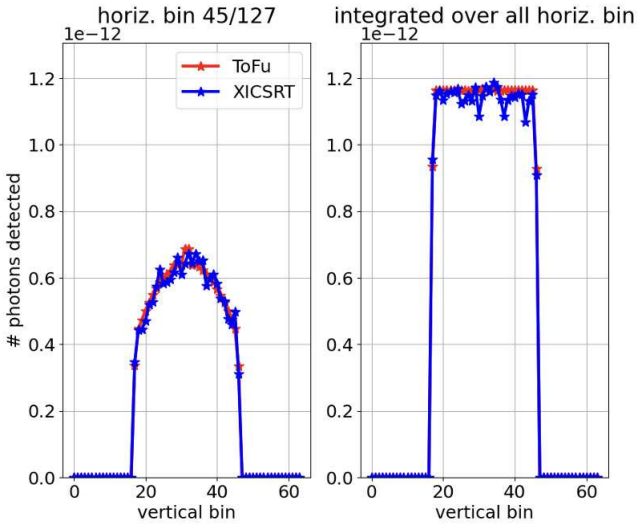

FIG. 3. Comparison of photon flux images between TOFU and XICSRT for an example spherical crystal spectrometer. The images are elliptically bent so the left plot is a slice over a particular horizontal pixel bin illustrating the same curvature while the right plot is integrated across horizontal pixel bins illustrating the same photon flux.

IV. ATOMIC DATA MODELING

Included in the spectra modeling is Bremsstrahlung and radiative recombination with free-free and bound-free (up to principal quantum number, $n = 6$) Gaunt factors sourced from the CHIANTIPY code[27–29]. Energy levels when calculating the radiative recombination of Kr and Xe are supplemented using the FLEXIBLE ATOMIC CODE (FAC)[30].

Cross-sections and decay rates for the line radiation emitted by Kr, Xe are sourced from FAC. The processes included in this work are spontaneous emission (over all multipoles), electron impact excitation, electron impact ionization, autoionization/dielectronic recombination, and radiative recombination. Collisional-radiative modeling is then performed using COLRADPY[31]. Care was taken to validate the generated data against what is available on OPENADAS[32,33] as well as in literature[34,35]. Note that since SPARC plasmas are expected to reach $T_e > 10keV$, a significant portion of the electron population approach relativistic energies ($E \sim m_e c^2$). FAC already solves for relativistic cross-sections, but when averaging that data into rate coefficients one must account for 1) the relativistic energy-velocity relation and 2) to a lesser extent that the maximal entropy energy distribution shifts from a Maxwell-Boltzmann to a Maxwell-Jüttner. Line radiation from other species is supplemented by what is available on OPENADAS.

Since the collisional-radiative modeling includes levels that mainly decay by two-photon emission, the continuum emission is modeled. H- and He-like rates are sourced from FAC. Energy distributions are then sourced from CHIANTIPY, but supplemented for Z >30[36,37].

Spectrum modeling is managed by the AURORA code[38,39]. All lines from Kr, Xe are Voigt broadened sourcing Einstein coefficients from FAC with other species being Doppler broadened. AURORA also manages calculating the charge state density distribution sourcing effective ionization and recombination data from OPENADAS. For this work, no transport was considered, but dramatically peaked/hollow profiles will be considered in future work. It is important to note that we have found the effective ionization/recombination rates posted on OPENADAS to not always be accurate compared to experiment. From experience doing similar such calculation for the charge state distribution of Mo in Alcator C-Mod[40], it would appear that excitation-autoionization processes were neglected in the atomic data modeling resulting in an underabundance of closed shell charge states and an overabundance of alkali-like states. In progress is recalculating these data, particularly for Ne-like Xe, similarly to what was done in[41].

Figure 4 illustrates a spectrum calculated for He-like Kr including Li-like satellites in good agreement with measured

spectra on TFTR[42]. For the He-like system, FAC was run with singly excited states up to $n = 10$ and doubly excited states $2lnl'$ up to $n \leq 6$ including all possible orbital angular momenta. For the Li-like system, FAC was run with singly excited states up to $n = 9$ and doubly excited states $1s2lnl'$ up to $n \leq 6$ including all possible orbital angular momenta. Note that at this time emissivities from only excitation and recombination are calculated with ionization to be included. Only two-photon emission was included for continuum radiation in this figure. Also shown in shaded magenta is a possible wavelength calibration source using second-order diffraction of the Sb K_α sequence[43].

V. PROFILE RECONSTRUCTIONS

Figure 5 depicts a synthetic detector image for a midplane beamline imaging He-like Kr produced from volume-of-sight integration with TOFU assuming the SPARC "Primary Reference Discharge" H-mode plasma[44]. The w line is the rightmost trace around horizontal bin 80. Note that bins are integrated over many pixels per candidate detector geometries. The viewed regions of the plasma gets hotter from the bottom to the top of the image illustrating the asymmetric instrumental broadening discussed in Section II.

Ion temperature and toroidal velocity reconstructions are being performed using the He-like Kr w line and Ne-like Xe 3D line, but will not be shared here in preference to a future publication. We will scope how well we can reconstruct profiles over an ensemble of L-/H-mode $n_e/T_e/T_i/n_{Kr/Xe}$ kinetic profiles, particular fictitious cases that are extremely hollow or peaked. Similarly, misalignments from the measured as-installed diagnostic geometry considering tilts and translations of optics with respect to each other will be explored. Care must be taken to include error bars from Poisson statistics[45] and spectral fitting.

An initial concern with reconstructing ion temperature was the strong nuclear charge scaling of the natural width, e.g. for optically allowed transitions $A_{ij} \sim Z^4$, where A_{ij} is the Einstein coefficient. Conveniently the full-width half-maximum due to Doppler broadening dominates that for a Lorentzian by a factor of five above $T_i = 5$ keV for He-like Kr ($A_w = 1.56e15$ s^{-1}) and above $T_i = 1$ keV for Ne-like Xe ($A_{3D} = 4.62e14$ s^{-1}). Well below the temperature range we can expect to have significant signal from the respective species. This allows to use reconstruction methods such as taking spectral moments of the detector image assuming it is a sum of Gaussians[46].

It is important to note that it is likely that not all 5 beamlines will be installed on SPARC immediately. The tentative plan for day one of operations is to have two beamlines closest to the midplane installed for a redundant measure of the line-averaged ion temperature. We may install for the second campaign another beamline furthest out towards the edge to establish a gradient. Full coverage should be available for SPARC's third campaign. This deployment plan clearly further constrains the spatial resolution of the reconstruction, so we are scoping the quality of measured ion temperature profiles given a certain subset of the beamlines.

Electron temperature reconstructions are also being explored. This has been shown possible for Ne-like Xe using Na- and Mg-like satellites on Alcator C-Mod[41]. Historically for He-like Ar, the ratio of the w line to the $n \geq 3$ or k satellites has been used, such as on WEST[14]. As can be seen in Figure 4, this may be challenging since the desired lines are buried by brighter lines.

Overlapping lines from other species, such as W, degenerate with our lines of interest is a significant concern when designing our reconstruction workflow. This has been shown to complicate analyzing He-like Ar spectra on tungsten-walled machines such as WEST[47]. Indeed if one looks at some of the photon emissivity coefficient files posted on OPENADAS it is implied there may be a degenerate Al-like W line with the Ne-like Xe 3D line. Theoretically calculated wavelengths are notoriously wrong though so we are exploring precise wavelength measurements of W in the Ne-like Xe spectral range of interest using the assistance of an Electron Beam Ion Trap (EBIT) facility.

VI. CONCLUSIONS

The final design of the SPARC X-ray crystal spectrometers is moving along with construction of the system beginning soon. Vendors have been identified for the various components discussed in the text with prototypes already received for review. Still we have illustrated atomic data needs to carefully scope spectrometer throughput and reliability to reconstruct kinetic profiles. Further optimization of the design to maximize performance and analysis is in progress.

CONFLICTS OF INTERESTS STATEMENT

All authors are financially supported by Commonwealth Fusion Systems (CFS) either as employees or through sponsored research contracts. CFS is seeking to commercialize fusion energy and may benefit financially from the science and technologies discussed in this manuscript.

ACKNOWLEDGEMENTS

The authors would like to thank N. Pablant (PPPL), L. Delgado-Aparicio (PPPL), K. Shah (PPPL), L. Gao (PPPL), G. Brown (LLNL), F. Bombarda (ENEA), T. Odstrčil (GA), M.F. Gu (U.C. Berkeley), A. Foster (Harvard), and O. Marchuk (IEK) for conversations in benefit to this work. This work is supported by Commonwealth Fusion Systems RPP031.

[1] J. Rice and *et al.*, Nuclear Fusion **44**, 379 (2004).
[2] J. Rice and *et al.*, Nuclear Fusion **47**, 1618 (2007).
[3] J. Rice and *et al.*, Nuclear Fusion **57**, 116004 (2017).
[4] A. Creely and *et al.*, Journal of Plasma Physics **86**, 865860502 (2020).
[5] M. Bitter and *et al.*, Physical Review Letters **42**, 304–307 (1979).
[6] E. Källne and *et al.*, Review of Scientific Instruments **31**, 551 (1985).
[7] M. Bitter and *et al.*, Review of Scientific Instruments **70**, 292 (1999).

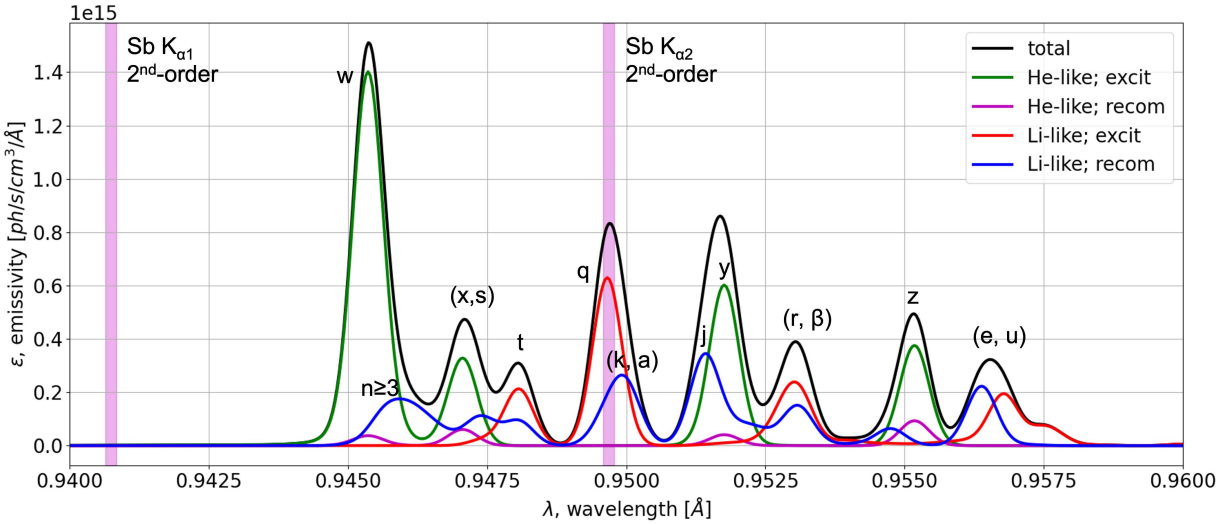

FIG. 4. Simulated He-like Kr spectrum including Li-like satellites using FAC/ColRadPy. The assumed plasma conditions are $T_e = T_i = 6.0keV$, $n_e = 10^{14} cm^{-3}$, $n_{Kr}/n_e = 10^{-3}$, and no impurity transport. All lines have been Voigt broadened.

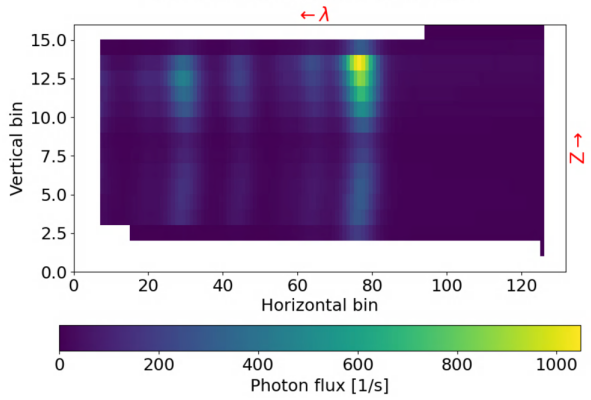

FIG. 5. Synthetic detector image from ToFu for a midplane beamline imaging He-like Kr, using an illustrative cylindrical crystal of radius 0.6 m (not the final radius). The plasma center is at the top. Spectral resolution vs throughput to be optimized in future works.

[8] J. Weinheimer and *et al.*, Review of Scientific Instruments **72**, 2566 (2001).
[9] M. Bitter and *et al.*, Physical Review Letters **42**, 304 (1978).
[10] P. Platz and *et al.*, Journal of Physics E: Scientific Instruments **14**, 448 (1981).
[11] R. Bartiromo and *et al.*, Nuclear Instruments and Methods in Physics Research **225**, 378–384 (1984).
[12] R. Bartiromo and *et al.*, Physical Review Letters **60**, 237 (1988).
[13] A. Ince-Cushman and *et al.*, Review of Scientific Instruments **79**, 10E302 (2008).
[14] A. D. Ros and *et al.*, Review of Scientific Instruments **95**, 043505 (2024).
[15] R. Barnsley and *et al.*, Review of Scientific Instruments **75**, 3743 (2004).
[16] L. Ingesson and *et al.*, Review of Scientific Instruments **75**, 3696 (2004).
[17] P. Beiersdorfer and *et al.*, Journal of Physics B: Atomic, Molecular and Optical Physics **43**, 144008 (2010).
[18] D. Lu and *et al.*, Review of Scientific Instruments **92**, 043544 (2021).
[19] Z. Cheng and *et al.*, Review of Scientific Instruments **93**, 073502 (2022).
[20] D. Vezinet and *et al.*, "SPARC X-ray diagnostics: technical and funcational overview," Review of Scientific Instruments (2024), **these proceedings**.
[21] L. von Hámos, Annalen der Physik **17**, 716 (1933).
[22] W. Zachariasen, *Theory of X-ray Diffracion in Crystals* (Dover Publications Inc, New York, NY, 1967).
[23] *International Tables for X-ray Crystallography*, Vol. 3 (The Kynoch Press, Birmingham, 1985).
[24] H. Chung and *et al.*, High Energy Density Physics **1**, 3–12 (2005).
[25] D. Vezinet and *et al.*, Nuclear Fusion **56**, 086001 (2016).
[26] N. Pablant and *et al.*, Review of Scientific Instruments **92**, 093904 (2021).
[27] K. Dere and *et al.*, Astronomy Astrophysics Supplement Series **125**, 149–173 (1997).
[28] K. Dere and *et al.*, The Astrophysical Journal Supplement Series **268**, 52 (2023).
[29] W. Karzas and R. Latter, Astrophysical Journal Supplement **6**, 167 (1961).
[30] M. Gu, Canadian Journal of Physics **86**, 675–689 (2008).
[31] C. Johnson and *et al.*, Nuclear Materials and Energy **20**, 100579 (2019).
[32] H. Summers and *et al.*, *The ADAS Manual v2.6* (2001).
[33] H. Summers and *et al.*, Plasma Physics and Controlled Fusion **48**, 263–293 (2006).
[34] R. Mewe, Astronomy and Astrophysics **20**, 215 (1972).
[35] R. Mewe and J. Schrijver, Astronomy and Astrophysics **65**, 99–114 (1978).
[36] S. Goldman and G. Drake, Physical Review A **24**, 183 (1981).
[37] A. Derevianko and W. Johnson, Physical Review A **56**, 1288 (1997).
[38] R. Dux, *Habilitation Thesis*, Phd thesis, MPI-IPP (2004).
[39] F. Sciortino and *et al.*, Plasma Physics and Controlled Fusion **63**, 112001 (2021).
[40] J. Rice and *et al.*, Journal of Physics B: Atomic, Molecular and Optical Physics **29**, 2191 (1996).
[41] J. Rice and *et al.*, Journal of Physics B: Atomic, Molecular and Optical Physics **53**, 055701 (2020).
[42] M. Bitter and *et al.*, Physical Review Letters **71**, 1007 (1993).
[43] Center for X-ray Optics and Advanced Light Source, *X-ray Data Booklet* (2009).
[44] P. Rodriguez-Fernandez and *et al.*, Journal of Plasma Physics **86**, 865860503 (2020).
[45] I. Hutchinson, The European Physical Journal Plus **127** (2012).
[46] M. Reinke and *et al.*, Review of Scientific Instruments **83**, 113504 (2012).
[47] J. Rice and *et al.*, Journal of Physics B: Atomic, Molecular and Optical Physics **54**, 095701 (2021).